PROCEEDINGS A

royalsocietypublishing.org/journal/rspa

Research

Check for updates

Article submitted to journal

Subject Areas:
Applied mathematics, Fluid mechanics

Keywords:
Hele-Shaw, Bubbles, Microfluidics, Conformal map, Complex potential, Thin films

Author for correspondence:
Ian Griffiths, Peter Howell
e-mail: ian.griffiths@maths.ox.ac.uk,
e-mail: howell@maths.ox.ac.uk

The motion of a bubble in a non-uniform Hele-Shaw flow

D. J. Booth, I. M. Griffiths, P. D. Howell

Mathematical Institute, University of Oxford, Andrew Wiles Building, Oxford, OX2 6GG, UK

We consider the propagation of a bubble in a non-uniform Hele-Shaw flow. We focus on a distinguished limit in which the bubble is approximately circular in plan view and its velocity is determined by a net force balance incorporating the Hele-Shaw viscous pressure and drag due to the thin films separating the bubble from the cell walls. We find that the instantaneous bubble velocity is the same as that for a bubble in a uniform flow given by the background fluid velocity evaluated at the bubble centre. We apply the model to common microfluidic components, such as a T-junction and injection sources and sinks. Using the same methodology, we derive approximate solutions for the motion of a bubble in more complicated domains including walls or obstacles. We validate the approximate approach with two test cases in which we can find the full solution analytically. First, we consider the effect of an impermeable wall on a bubble in a stagnation-point flow. Second, we consider the motion of a bubble around a circular obstacle. In both cases, the bubble deviates noticeably from the streamlines of the background flow only when it is very close to the wall or the obstacle.

1. Introduction

Many microfluidic systems involve the propagation of bubbles through a Hele-Shaw cell [1–4]. In this work, we focus on the motion of a single bubble whose diameter is much larger than the cell height, so it is flattened into a pancake-like shape, with thin liquid films separating the bubble from the walls of the cell [5,6]. Furthermore, we consider regimes in which the capillary number is small enough for the plan-view shape of the bubble to remain approximately circular. Booth *et al.* [7] present a model for the motion of such a bubble in a uniform background velocity.

THE ROYAL SOCIETY PUBLISHING

The dynamics of bubbles in a Hele-Shaw cell is both a classical fluid dynamics problem [8–11] and a fundamental mathematical problem due to its connection to potential theory and complex analysis [12–16]. For example, Taylor and Saffman [8] use conformal mapping techniques to show that a circular bubble in a uniform flow travels at twice the background flow speed in a regime where the Laplace pressure at the bubble interface is effectively constant. Crowdy [17] uses complex variable methods to study multiple co-travelling bubbles in an infinite Hele-Shaw cell. Andersen *et al.* [18] use exponential asymptotics and complex variable techniques to explore solution selection in the formation of viscous fingers in a wedge.

In their seminal work, Bretherton [19] shows that the presence of thin liquid films above and below a bubble in a capillary tube or Hele-Shaw cell gives rise to an additional pressure drop across the menisci of the bubble. Meiburg [20] incorporates this additional pressure drop in a numerical study of the shape of a bubble in a uniform background flow. Booth *et al.* [7] use the boundary condition derived by Meiburg to develop a general theory for the motion of approximately circular bubbles in a Hele-Shaw cell.

However, most of the aforementioned work involves the study of a bubble in a uniform background flow, while microfluidic devices generally involve a non-uniform background flow. Such flows can be generated, for example, by a T-junction [21–23] or by injecting fluid in one place and removing it at another [24]; the former situation can be modelled mathematically as a stagnation-point flow while the latter may be modelled using point sources and sinks. In this paper, we therefore extend the model derived in [7] to encompass non-uniform background flow conditions, obtaining a general equation of motion using complex variable methods similar to the Milne-Thompson Circle Theorem [12]. To the best of our knowledge there has been no previous theory to describe the motion of a bubble in a general non-uniform background flow.

In many physically relevant scenarios, cell walls or obstacles are present and have a significant impact on the bubble dynamics [4,21–23,25]. For example, Booth *et al.* [7] show that the presence of a wall can either increase or decrease the speed of a bubble in a Hele-Shaw cell, depending on the flow parameters. Shen *et al.* [26] show that a pair of bubbles can be reflected by a single wall, and "bounce" between two parallel walls. We adapt our methodology to derive approximate solutions for the motion of a bubble in these more complicated domains. Accurate prediction of the bubble trajectories will aid the fabrication of devices for bubble sorting or microfluidic bubble logic [4].

The structure of this paper is as follows. In §2, we present the governing equations and use a complex variable framework to find the analytic equation of motion for a bubble in a general unconfined non-uniform flow. Examples of the solution are presented in §3, for the experimentally relevant regimes of stagnation-point flow, and flow driven by point sources and sinks. In §4 we use the methodology to derive an approximate law of motion for a bubble in more complicated scenarios including walls or obstacles. We then compare the approximate solution with the full analytical solution in two examples. First, we explore the dynamics of a bubble near a stagnation point on an impermeable wall. Then, we consider the flow of a bubble around a circular obstacle. Finally, in §5 we summarise our key findings.

2. Motion of a bubble in an infinite domain

(a) Governing equations

We consider the motion of a bubble in a Hele-Shaw cell of height $\hat{h}$ parallel to the $(\hat{x}, \hat{y})$-plane. Here $\hat{h}$ is assumed to be much smaller than the horizontal dimensions of the cell so that we can employ lubrication theory. The bubble is flattened by the cell walls above and below, causing it to have a pancake-like shape and an approximately circular profile when viewed from above. The bubble is subject to a non-uniform background flow with a characteristic background velocity $\hat{U}$. The viscosity of the liquid and the liquid–air surface tension are denoted by $\hat{\mu}$ and $\hat{\gamma}$, respectively.

We non-dimensionalise the system by scaling lengths with a typical bubble radius $\hat{R}$, the depth-averaged fluid velocity $\hat{\boldsymbol{u}}$ with $\hat{U}$, the fluid pressure $\hat{p}$ with $12\hat{\mu}\hat{U}\hat{R}/\hat{h}^2$, and time, $\hat{t}$ with $\hat{R}/\hat{U}$. Dimensionless variables are denoted without hats. There are two dimensionless parameters associated with our problem, the aspect ratio and the capillary number, defined by

$$\epsilon = \frac{\hat{h}}{2\hat{R}}, \qquad \mathrm{Ca} = \frac{\hat{\mu}\hat{U}}{\hat{\gamma}}, \tag{2.1}$$

respectively, both of which are assumed to be small. Specifically, we consider the distinguished limit in which $\mathrm{Ca} = O(\epsilon^3)$ as $\epsilon \to 0$, so the viscous lubrication pressure balances the corrections to the pressure drop across the menisci calculated by Bretherton [19]. In this regime, the bubble remains circular to leading order [7].

In the Hele-Shaw approximation, we have $\boldsymbol{u} = -\nabla p$, where the dimensionless pressure satisfies Laplace's equation and a kinematic boundary condition on the bubble surface. To close the system we supply an effective net force balance between the Hele-Shaw viscous pressure and the pressure drop due to the thin films above and below the bubble [7], given by

$$-\frac{\delta}{\pi}\oint_{\partial\Omega_b} p\boldsymbol{n}\,\mathrm{d}s = \frac{\boldsymbol{U}_b}{|\boldsymbol{U}_b|^{1/3}}. \tag{2.2}$$

Here $\boldsymbol{U}_b = (U_b, V_b)$ is the bubble velocity, $\boldsymbol{n}$ denotes the unit normal, and δ is the *Bretherton parameter* [7], defined by

$$\delta = \frac{1}{\eta}\frac{\mathrm{Ca}^{1/3}}{\epsilon} = O(1), \tag{2.3}$$

where the numerical constant $\eta \approx 0.893$ incorporates the coefficients calculated by Bretherton for the pressure drops across the advancing and retreating menisci [19,27]. We note that the pressure drops derived by Bretherton depend only on the normal velocity of the bubble interface relative to the cell walls, and the equation of motion (2.2) is therefore unaffected by non-uniformity in the background flow (see, for example, [28]).

Since the pressure, p, satisfies Laplace's equation we can formulate the problem for a complex potential $w(z) = -p(x,y) + \mathrm{i}\psi(x,y)$, where ψ is the dimensionless streamfunction and $z = x + \mathrm{i}y$. If we denote the *a priori* unknown position of the bubble centre by $z = c(t)$, then the complex representation of the bubble velocity $\mathcal{U}_b = U_b + \mathrm{i}V_b = \dot{c}$, where the dot represents differentiation with respect to t. Given $c(t)$ and $\dot{c}(t)$ at time t, the complex potential is instantaneously determined (up to an arbitrary real constant) by imposing the prescribed non-uniform flow in the far field and the kinematic boundary condition on the bubble interface, namely

$$\boldsymbol{u}\cdot\boldsymbol{n} = \boldsymbol{U}_b\cdot\boldsymbol{n} \qquad \text{on} \quad |z-c| = 1. \tag{2.4}$$

Here, we have neglected leakage into the thin films because the effect is always subdominant, contributing corrections of order $\mathrm{Ca}^{2/3}$ to the kinematic condition (2.4) (see, for example, [27,29,30]). In complex variables, $\boldsymbol{n}$ can be represented by $-\mathrm{i}\mathrm{d}z/\mathrm{d}s$, where s denotes arc-length, and $\mathrm{d}w/\mathrm{d}z = u - \mathrm{i}v$. Thus we can rewrite (2.4) as

$$\mathrm{Im}\left[\frac{\mathrm{d}w}{\mathrm{d}z}\frac{\mathrm{d}z}{\mathrm{d}s}\right] = \mathrm{Im}\left[\overline{\mathcal{U}}_b\frac{\mathrm{d}z}{\mathrm{d}s}\right] \qquad \text{on} \quad |z-c| = 1, \tag{2.5}$$

where the over-bar represents complex conjugation. As noted above, we consider a regime in which the bubble remains circular to leading order, and it follows that $\mathcal{U}_b = \dot{c}$ is independent of s, so we can integrate (2.5) to obtain

$$\mathrm{Im}[w(z)] = q + \mathrm{Im}\left[\bar{\dot{c}}(z-c)\right] \qquad \text{on} \quad |z-c| = 1, \tag{2.6a}$$

where q is an arbitrary real constant (or function of t). Finally, supposing that, without the bubble present, we have a background flow with (dimensionless) complex potential $f(z)$, we impose the

external condition

$$w(z) \text{ has the same singularities as } f(z) \text{ in } |z-c|>1. \tag{2.6b}$$

(2.6*a*) (2.6*b*)

Assuming we have evaluated the complex potential $w(z)$ satisfying (2.6), we find an ordinary differential equation for $c(t)$ by performing the effective net force balance (2.2) on the bubble, which leads to

$$\frac{1}{\mathrm{i}\pi}\oint_{|z-c|=1} w(z)\,\mathrm{d}z = \dot{c}\left(-1+\frac{1}{\delta|\dot{c}|^{1/3}}\right). \tag{2.7}$$

(b) Equation of motion

For scenarios of interest, $f(z)$ will have no singularities in $|z-c|\le 1$, (since we assume that the bubble cannot intersect with any external fluid sources, sinks, or obstacles). Then we can write $w(z)=f(z)+W(z)$, where

- $\mathrm{Im}[W(z)] = \mathrm{Im}\left[\bar{\dot{c}}(z-c)-f(z)\right]$ on $|z-c|=1$, (2.8*a*)
- $W(z)$ is holomorphic and bounded in $|z-c|>1$. (2.8*b*)

Here, without loss of generality, we have set $q=0$, which means that $W(z)$, although bounded, does not in general tend to zero as $z\to\infty$.

Since $(z-c)(\overline{z}-\overline{c})=1$ on the bubble surface, we can rewrite the kinematic boundary condition (2.8*a*) as

$$\mathrm{Im}[W(z)] = \mathrm{Im}\left[\overline{f}\left(\overline{c}+\frac{1}{z-c}\right)-\frac{\dot{c}}{z-c}\right] \qquad \text{on} \quad |z-c|=1, \tag{2.9}$$

where $\overline{f}(z)=\overline{f(\overline{z})}$ is the conjugate function to f. Recall that all the singularities of $f(z)$ are assumed to be in $|z-c|>1$, so the term in the square brackets on the right-hand side of (2.9) is holomorphic in $|z-c|>1$ and we have the solution

$$w(z) = f(z)+\overline{f}\left(\overline{c}+\frac{1}{z-c}\right)-\frac{\dot{c}}{z-c}, \tag{2.10}$$

up to an irrelevant constant.

Evaluating the force balance (2.7) gives

$$\frac{1}{\mathrm{i}\pi}\oint_{|z-c|=1}\left[f(z)+\overline{f}\left(\overline{c}+\frac{1}{z-c}\right)-\frac{\dot{c}}{z-c}\right]\mathrm{d}z = \dot{c}\left(-1+\frac{1}{\delta|\dot{c}|^{1/3}}\right). \tag{2.11}$$

By Cauchy's Residue Theorem, the first term in the integral in (2.11) evaluates to 0, and the last term evaluates to $-2\dot{c}$. To manipulate the middle term of the integral into a suitable form for Cauchy's Residue Theorem, we take the conjugate and use $\mathrm{d}\overline{z}=-\mathrm{d}z/(z-c)^2$ to obtain

$$\frac{1}{\mathrm{i}\pi}\oint_{|z-c|=1}\frac{f(z)}{(z-c)^2}\,\mathrm{d}z = \bar{\dot{c}}\left(1+\frac{1}{\delta|\dot{c}|^{1/3}}\right). \tag{2.12}$$

The left-hand side can now be evaluated to obtain the equation of motion

$$2\overline{f'(c)} = \dot{c}\left(1+\frac{1}{\delta|\dot{c}|^{1/3}}\right). \tag{2.13}$$

Since the velocity of the background flow is given by $u-\mathrm{i}v=f'(z)$, equation (2.13) implies that the bubble goes with the flow, with its velocity proportional to the background velocity evaluated at the centre of the bubble. Thus, the bubble travels along a streamline of the flow that would exist if the bubble were not present. Unlike a tracer particle, however, the bubble moves at a different speed from the background flow.

By taking the absolute value of each side of (2.13), we obtain the universal relation

$$2u_f = u_b + u_b^{2/3}, \tag{2.14}$$

between $u_f = \delta^3|f'(c)|$ and $u_b = \delta^3|\dot{c}|$, which are the dimensionless speeds of the background flow and the bubble at $z = c$, respectively, when we choose the characteristic velocity $\hat{U}$ such that $\delta = 1$. We plot the prediction (2.14) for the bubble speed versus the background flow speed in figure 1. We observe that u_b is a monotonic increasing function of u_f. As $u_f \to 0$ we find that $u_b \sim (2u_f)^{3/2}$, while $u_b \sim 2u_f$ as $u_f \to \infty$. Thus the Taylor–Saffman prediction [8], that a circular bubble travels at twice the background flow speed, is recovered when the background flow is sufficiently fast.

If we define the relative speed of the bubble compared to the background velocity at the bubble centre as $U_{\text{rel}} = u_b/u_f = |\dot{c}| \,/\, |f'(c)| > 0$, then (2.14) may be expressed in the form

$$\frac{U_{\text{rel}}^{2/3}}{2 - U_{\text{rel}}} = u_f^{1/3} = \delta\,|f'(c)|^{1/3} =: \Delta(c). \tag{2.15}$$

First consider the simplest non-trivial case of a uniform background flow, which can be used to describe pressure-driven flow through a Hele-Shaw channel (see, for example, [31,32]). The dimensionless complex potential is $f(z) = z$, so $f'(z) \equiv 1$ and (2.15) reduces to

$$\frac{U_b^{2/3}}{2 - U_b} = \delta, \tag{2.16}$$

where now $|\dot{c}| = U_b$ is the bubble speed relative to the constant background flow speed. The relation (2.16) was obtained by Booth *et al.* [7] for a bubble in a uniform flow and has now been extensively validated experimentally [27]. The generalised relation (2.15) is equivalent to (2.16) when the bubble velocity is measured relative to the *local* flow speed and $\Delta(c)$ is interpreted as the *local* value of the Bretherton parameter, based on the background flow velocity evaluated at the bubble centre $z = c$.

To illustrate how the general theoretical result (2.13) works in practice, in the next section we apply it to two examples relevant to microfluidic devices: stagnation-point flow, and flow due to a point source and sink. In both situations, the bubble trajectories can be explicitly stated, allowing for easy calculation of U_{rel} from (2.15) and providing physical insight into how the motion of a bubble varies with position in these commonly encountered flows.

3. Examples

(a) Stagnation-point flow

Next, we consider stagnation-point flow, which has the complex potential $f(z) = z^2$, with appropriate non-dimensionalisation. This background velocity can be used to simulate the flow in a T-junction or a cross-junction, which are common components in microfluidic systems (see, for example, [21–23]). In this case, (2.13) becomes

$$4\overline{c} = \dot{c}\left(1 + \frac{1}{\delta|\dot{c}|^{1/3}}\right). \tag{3.1}$$

A streamline in the positive quadrant (without loss of generality) is given by the hyperbola $xy = a^2$ for some constant $a \geq 0$. The path followed by a bubble can thus be parametrised by

$$c(t) = a\left(\mathrm{e}^{\phi(t)} + \mathrm{i}\mathrm{e}^{-\phi(t)}\right), \tag{3.2}$$

where

$$\dot{\phi}\left[1 + \frac{1}{\delta a^{1/3}|\dot{\phi}|^{1/3}(2\cosh 2\phi)^{1/6}}\right] = 4. \tag{3.3}$$

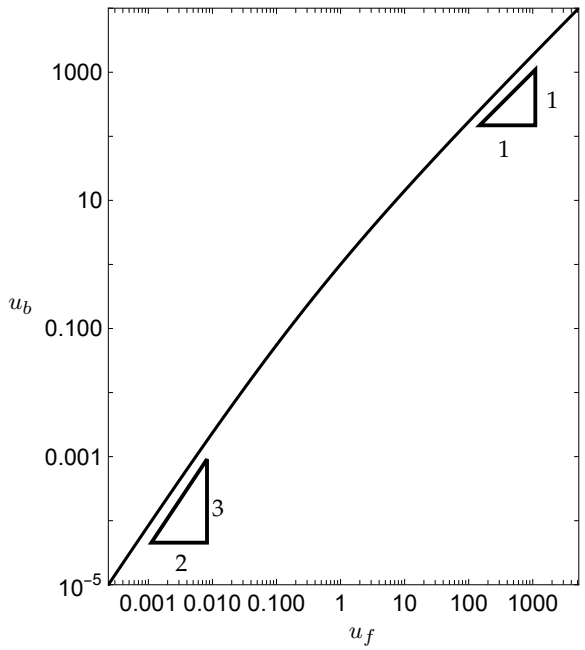

Figure 1. The normalised speed of the bubble, u_b, versus the normalised speed of the background flow, u_f, on log–log axes. When $u_f \to 0$, $u_b \sim (2u_f)^{3/2}$ and as $u_f \to \infty$, $u_b \sim 2u_f$.

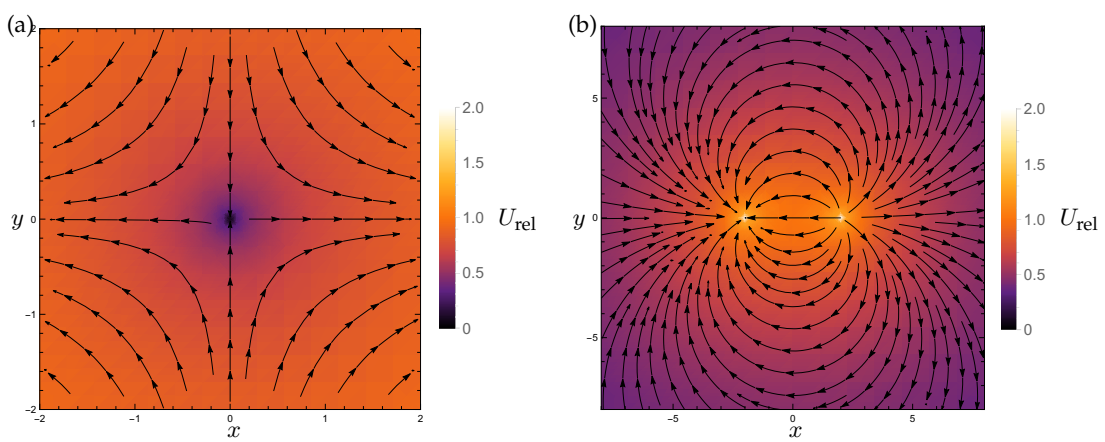

Figure 2. Trajectories of the bubble centre, c, in (a) a stagnation-point flow with $\delta = 0.5$, (b) flow between a point source and sink with $s = 2$ and $\delta = 1$. The colour bars show the value of U_{rel}, given by (2.15).

In figure 2(a) we overlay trajectories of (3.1) on a density plot of the relative bubble speed U_{rel}, given by (2.15). We observe that $U_{\text{rel}} \to 2$ as $|c| \to \infty$, i.e., where the background flow is very fast, the bubble travels approximately twice as fast. On the other hand, $U_{\text{rel}} \to 0$ as $|c| \to 0$, i.e., as the background flow speed approaches zero, the bubble speed decreases to zero even more rapidly. In particular, for a bubble travelling along $x = 0$, the bubble centre will approach the origin but not reach it in finite time.

(b) Point source and sink

In many microfluidic devices, fluid is injected into the Hele-Shaw cell via a syringe and then removed similarly at some point downstream [24]. The resulting flow can be modelled using a point source and sink of equal strength some distance apart. Without loss of generality, we may place the singularities at $z = \pm s \in \mathbb{R}$, so the complex potential for the flow is given by

$$f(z) = \log(z - s) - \log(z + s), \tag{3.4}$$

with suitable non-dimensionalisation. For this system, (2.13) becomes

$$2\left(\frac{1}{\bar{c} - s} - \frac{1}{\bar{c} + s}\right) = \dot{c}\left(1 + \frac{1}{\delta|\dot{c}|^{1/3}}\right). \tag{3.5}$$

The streamlines are circular arcs on which

$$c(t) = h\mathrm{i} + \sqrt{h^2 + s^2}\mathrm{e}^{\mathrm{i}\phi(t)}, \tag{3.6}$$

for constant $h \in \mathbb{R}$, and where $\phi(t)$ satisfies

$$\frac{2s}{(h^2 + s^2)(h + \sqrt{h^2 + s^2}\sin\phi)} = \dot{\phi}\left[1 + \frac{1}{\delta|\dot{\phi}|^{1/3}(h^2 + s^2)^{1/6}}\right]. \tag{3.7}$$

In figure 2(b) we overlay trajectories of (3.5) on a density plot of U_{rel}. In contrast with the stagnation-point example, now the background flow velocity tends to zero far from the source–sink pair, so likewise U_{rel} tends to zero and hence the bubble velocity tails off even more rapidly in the far field. We also observe that $U_{\mathrm{rel}} \to 2$ as $c \to \pm s$, so the bubble travels faster than the background flow in a neighbourhood of the source or sink.

4. Flows with boundaries

(a) Approximate solutions

So far, all of our solutions are for a bubble in an infinite Hele-Shaw cell. In many physical situations, cell walls or obstacles are present and have a significant impact on the bubble dynamics (see §1). In these situations, the solution found in §2(b) is no longer valid. Furthermore, an analytical solution is no longer possible in general due to the more complicated geometry. However, we can use the methodology developed in §2(b) to derive an approximate equation of motion for a bubble in a more complicated domain, including cell walls or obstacles. We construct the approximate solution as follows:

(*i*) find the complex potential $f(z)$ of the flow without the bubble present;

(*ii*) use (2.13) as an approximate equation of motion for the bubble.

This approximation is equivalent to assuming that the image contributions due to the presence of the bubble are negligible, so the bubble follows but does not affect the streamlines of the background flow. Similar approximations are employed to study the dynamics of a large number of bubbles in a uniform background flow using dipole models (see, for example, [26,31,33]).

The advantage of such an approximation is that one only needs to find the complex potential of the background flow once, from which the equation of motion for the bubble is found once and for all. In contrast, for the full solution, one needs to calculate the complex potential in the evolving multiply-connected domain at each time step, which is much more laborious.

In the next two subsections, we will compare the approximate solution described above with two scenarios in which we can find the full solution analytically. First, we consider a stagnation-point flow with an impermeable wall. Then we consider the flow of a bubble around a circular obstacle. In both cases, we compare the instantaneous bubble velocities predicted by the approximate and the full solution, as well as the transit times of a bubble (until either collision

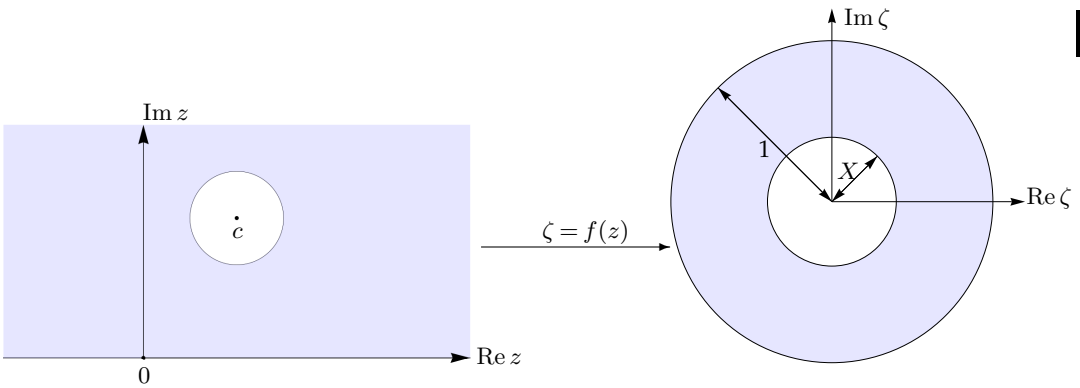

Figure 3. Schematic of the conformal map $\zeta = f(z)$ (4.2) from the fluid region, Ω, to the annulus $\{\zeta : X \leq |\zeta| \leq 1\}$.

with the wall or successful navigation around the obstacle). The instantaneous bubble velocities provide local information about the effect of the boundaries on the bubble motion, while the transit times provide a useful diagnostic of the global influence of the boundaries on the bubble dynamics. In particular, we will see that small local errors in the instantaneous velocity when the bubble is close to an obstacle do not in general accumulate to significantly affect the global bubble trajectory. In practice, accurate control of bubble transit times is essential in complex microfluidic components such as logic gates [4].

(b) Bubble near a stagnation point on a wall

(i) Solution

Returning to the stagnation-point flow introduced in §3(a), we now include an impermeable wall along the real axis through the stagnation point. This setup provides a simple model for a bubble passing through a T-junction in a microfluidic device. The presence of the wall does not affect the background complex potential $f(z) = z^2$, so the approximate equation of motion for the bubble, as described in §4, is still given by (3.1).

To find the full solution, we seek a complex potential $w(z)$ which is a holomorphic function that satisfies the boundary conditions

$$\mathrm{Im}[w(z)] = q + \mathrm{Im}\left[\overline{\mathcal{U}}_b(z-c)\right] \qquad \text{on} \quad |z-c| = 1, \tag{4.1a}$$

$$\mathrm{Im}[w(z)] = 0 \qquad \text{on} \quad \mathrm{Im}(z) = 0, \tag{4.1b}$$

$$w(z) \sim z^2 \qquad \text{as} \quad z \to \infty, \tag{4.1c}$$

where the complex bubble velocity is again denoted by $\mathcal{U}_b = \dot{c}$. We adapt the approach used by Booth *et al.* [7] by conformally mapping the solution domain, Ω, onto a concentric annulus (see figure 3), where the problem becomes solvable with standard techniques. Following the mapping

$$\zeta = f(z) = \frac{z - \alpha - \mathrm{i}\sqrt{\beta^2 - 1}}{z - \alpha + \mathrm{i}\sqrt{\beta^2 - 1}}, \tag{4.2}$$

where $c = \alpha + \mathrm{i}\beta$, the solution domain in the ζ-plane is $A = \{\zeta : X < |\zeta| < 1\}$, where

$$X = \beta - \sqrt{\beta^2 - 1}. \tag{4.3}$$

If we write the complex potential in the form $w(z) = z^2 + W(f(z))$, then $W(\zeta)$ is a holomorphic function on the annulus A and satisfies the boundary conditions

$$\mathrm{Im}[W(\zeta)] = 0 \qquad \text{on} \quad |\zeta| = 1, \tag{4.4a}$$

$$\mathrm{Im}[W(\zeta)] = q + \mathrm{Im}\left[\rho\left(\frac{1+\zeta}{1-\zeta}\right) + \nu\left(\frac{1+\zeta}{1-\zeta}\right)^2\right] \qquad \text{on} \quad |\zeta| = X, \tag{4.4b}$$

where $\rho = (2\alpha - \overline{\mathcal{U}_b})\mathrm{i}\sqrt{\beta^2-1}$ and $\nu = \beta^2 - 1$. We expand $W(\zeta)$ as a Laurent series to obtain

$$W(\zeta) = -\sum_{n=1}^{\infty} \frac{X^{2n}}{1-X^{2n}}\left[(4n\nu + 2\rho)\zeta^n + (4n\nu + 2\overline{\rho})\zeta^{-n}\right]. \tag{4.5}$$

Evaluating the left-hand side of the force balance (2.7) and using Cauchy's Residue Theorem we find

$$\frac{1}{\mathrm{i}\pi}\oint_{\partial\Omega_b} w(z)\,\mathrm{d}z = -4\mathrm{i}\sqrt{\beta^2-1}\sum_{n=1}^{\infty}\frac{nX^{2n}}{1-X^{2n}}(4n\nu + 2\overline{\rho}), \tag{4.6a}$$

$$= -\frac{2\sqrt{\beta^2-1}}{(\log X)^3}\left((\beta^2-1)\mathrm{i}\Psi''_{X^2}(1) + (2\alpha - \mathcal{U}_b)\sqrt{\beta^2-1}\Psi'_{X^2}(1)\log X\right), \tag{4.6b}$$

where we have rewritten the sums in terms of the q-digamma function, Ψ [34]. The equation of motion (2.7) can then be written as

$$F_1(c) = \mathcal{U}_b\left(F_2(\beta) + \frac{1}{\delta|\mathcal{U}_b|^{1/3}}\right), \tag{4.7}$$

where

$$F_1(\alpha + \mathrm{i}\beta) = -\frac{2\mathrm{i}\left(\beta^2-1\right)^{3/2}}{(\log X)^3}\Psi''_{X^2}(1) + \frac{4\alpha\left(\beta^2-1\right)}{(\log X)^2}\Psi'_{X^2}(1), \tag{4.8a}$$

$$F_2(\beta) = -1 + \frac{2\left(\beta^2-1\right)}{(\log X)^2}\Psi'_{X^2}(1). \tag{4.8b}$$

(ii) Results

One can verify that $F_1(c) \sim 4\overline{c}$ and $F_2(\beta) \to 1$ as $\mathrm{Im}[c] = \beta \to \infty$, and thus the full equation of motion (4.7) is indeed approximated by (3.1) when the bubble is sufficiently far from the wall. As demonstrated in figure 4, we find that the bubble trajectories continue to closely follow the streamlines of the background flow until the bubble is extremely close to the wall. Recall that the bubble has unit dimensionless bubble radius, so the bubble intersects the wall when $\beta = 1$. The trajectory shown in figure 4 therefore departs noticeably from the corresponding streamline only when the bubble is less than about a quarter radius from the wall. We note that the Hele-Shaw model will ultimately break down and three-dimensional effects will become important when $\beta - 1 = O(\epsilon)$.

To distinguish between the full and approximate solutions, we denote by $\mathcal{U}_b = U_b + \mathrm{i}V_b$ and $\mathcal{U}_{\text{approx}} = U_{\text{approx}} + \mathrm{i}V_{\text{approx}}$ the bubble velocities predicted by (4.7) and by the approximate equation (3.1), respectively. We compare the directions of motion predicted by the two theories by computing the velocity ratio

$$U_{\text{ratio}} = \frac{V_b/U_b}{V_{\text{approx}}/U_{\text{approx}}} = -\frac{\alpha V_b}{\beta U_b} = \frac{\sqrt{\beta^2-1}\Psi''_{X^2}(1)}{2\beta\Psi'_{X^2}(1)\log X}. \tag{4.9}$$

This ratio is solely a function of the distance β from the wall, and is plotted in figure 5. It is a monotonically increasing function of β with $U_{\text{ratio}} \to 1$ as $\beta \to \infty$, and $U_{\text{ratio}} \to 6\mathcal{Z}(3)/\pi^2$ as $\beta \searrow 1$, where $\mathcal{Z}(s)$ is the zeta-function. The former limit means the trajectories follow the streamlines of the background flow far away from the wall; deviations of over 5% occur only when the bubble is

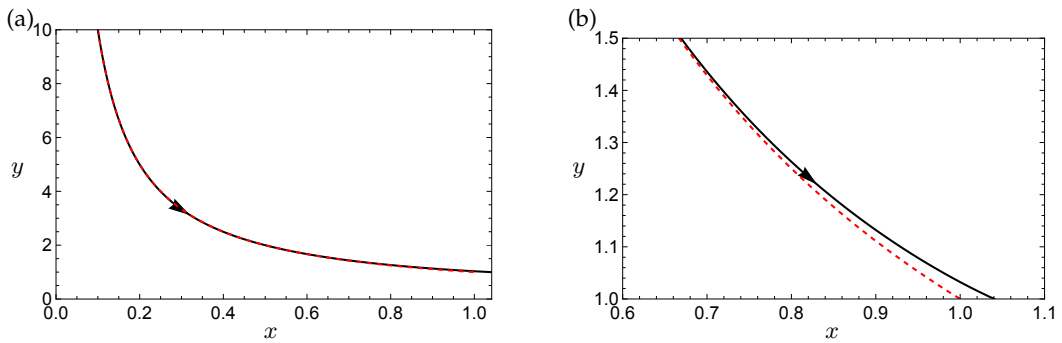

Figure 4. (a): A trajectory of (4.7) (black) with $\delta = 1$ and the corresponding streamline of the background flow (red, dashed). (b) The trajectory zoomed into the range $x \in [0.6, 1.1]$.

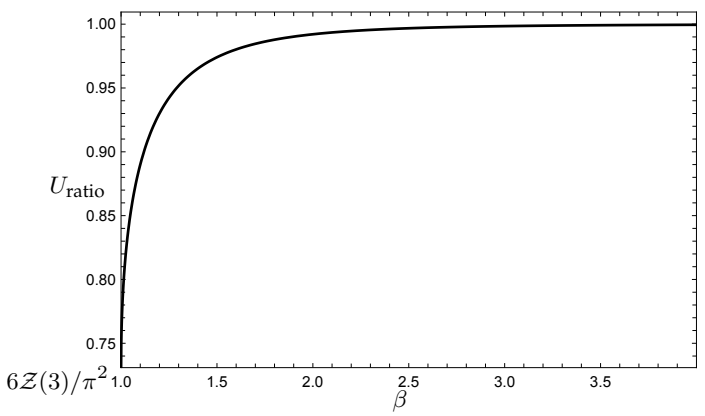

Figure 5. Velocity ratio U_{ratio} given by (4.9) versus distance of the bubble centre from the wall, β.

less than approximately 0.3 radii away from the wall. The latter limit means the bubble still has a non-zero velocity perpendicular to the wall as it approaches the wall and thus will always collide with the wall in finite time.

In figure 6 we plot the time for collision against δ for initial bubble positions of the form $k(0.1 + 10\text{i})$ with three different values of k. In each case, the bubble starts far enough from the wall to closely follow a streamline initially, and k labels which streamline it is on. We observe that the time taken for collision decreases with δ, because the bubble speed increases with δ. We also observe that the approximate solution ignoring the wall underestimates the time taken for a collision to occur. The presence of the wall thus provides some repulsive influence on the approaching bubble (also indicated by the weak singularity as $\beta \searrow 1$ in figure 5), but not strong enough to prevent finite-time collision.

To further quantify the difference between the full and approximate solutions we define the relative error as

$$\text{Error}(\beta) = \max_{\alpha \in \mathbb{R}} \frac{|\mathcal{U}_b - \mathcal{U}_{\text{approx}}|}{|\mathcal{U}_b|}. \tag{4.10}$$

We plot the error defined by (4.10) versus δ in figure 7, for various values of β. The maximum error is found to occur when $\beta = 1$, as expected because in this limit the bubble is touching the wall. However, as β is increased the error quickly decreases, with the error being at most 0.1 when $\beta = 2$. We find three regions of interest: as δ increases from zero, the error initially decreases, then remains constant for intermediate values of δ, before increasing again at large δ.

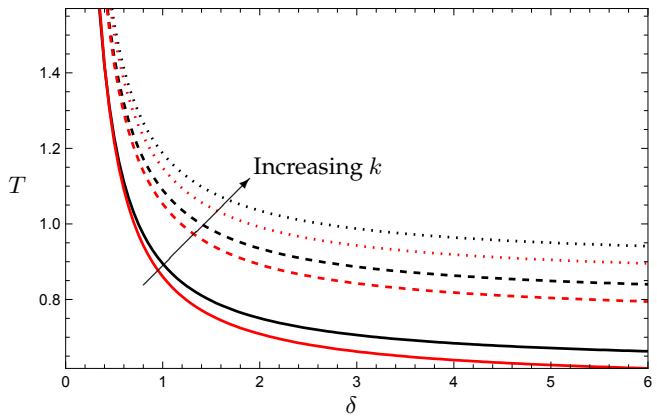

Figure 6. Time taken for a bubble to collide with the solid wall at $\mathrm{Im}(z) = 0$ versus δ, for a stagnation-point flow including wall effects (black) and with no wall (red). The bubble centre is initially at $z = k(0.1 + 10\mathrm{i})$ with $k = 1$ (solid curves), $k = 2$ (dashed curves), and $k = 3$ (dotted curves).

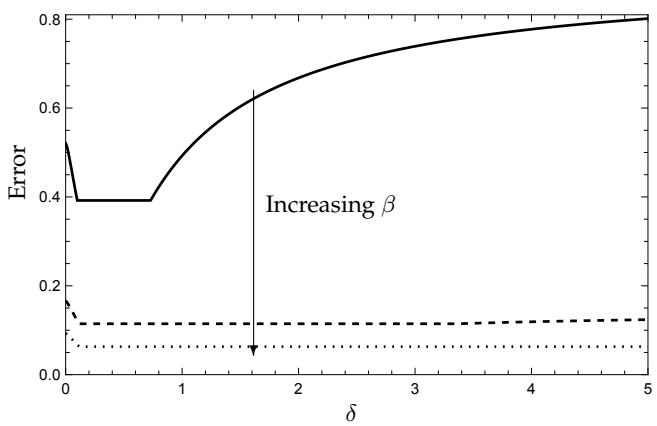

Figure 7. The maximum error in the bubble velocity for stagnation-point flow versus δ at fixed values of $\beta = 1$ (solid), 1.5 (dashed), 2 (dotted).

To explain this behaviour, in figure 8 we plot the bubble velocity components (U_b, V_b) and the corresponding approximations $(U_{\text{approx}}, V_{\text{approx}})$ versus α, with $\beta = 1$ and three different values of δ in each of the three regions identified above. In each case, because we keep $\beta = 1$ constant, the error is dominated by the behaviour of $|U_b - U_{\text{approx}}|$, and the errors in V_b are much smaller, except near $\alpha = 0$, because $U_b \gg V_b$ as $\alpha \to \infty$ (see (4.7) and (4.8)). In the small δ regime (see figure 8(a)) we find that $U_{\text{approx}} < U_b$ for small values of α. However we can calculate the limit

$$\frac{U_{\text{approx}}}{U_b} \to 2 - \frac{6}{\pi^2} > 1 \qquad \text{as} \quad \alpha \to \infty, \tag{4.11}$$

so the two graphs must cross over at some value of $\alpha = \alpha^*$, say. For small values of δ, the maximum error occurs within the region $0 < \alpha < \alpha^*$. However, as δ is increased (see figure 8(b)), the value of α^* decreases until the maximum error occurs at $\alpha = \infty$ (and is therefore constant). Finally, as δ is further increased, α^* reaches zero so $U_b < U_{\text{approx}}$ everywhere (see figure 8(c)), and the largest relative error now occurs at $\alpha = 0$.

(c) Motion of a bubble past a circular obstacle

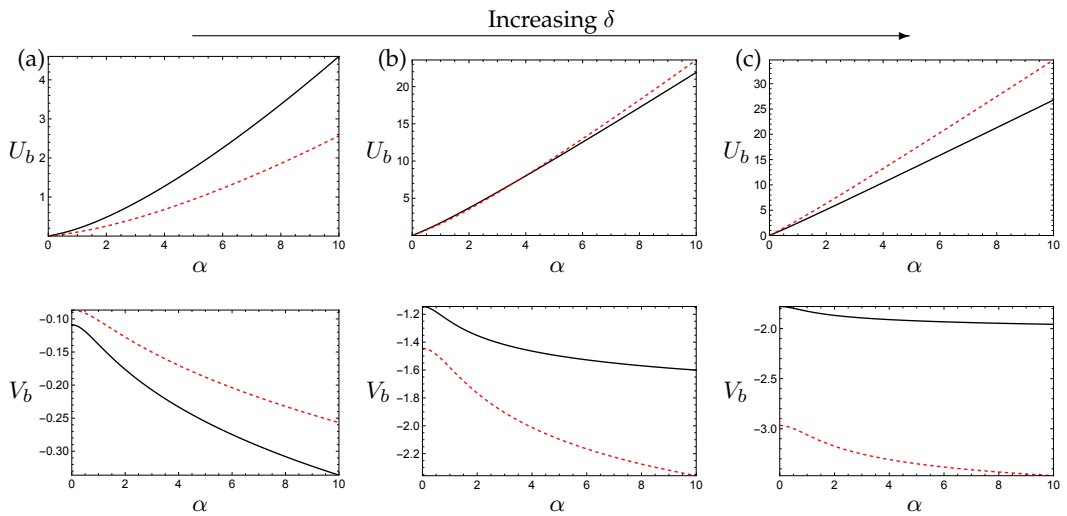

Figure 8. Instantaneous bubble velocity (U_b, V_b) (shown in top and bottom graphs, respectively) versus α, with $\beta = 1$, and (a) $\delta = 0.05$, (b) $\delta = 0.5$, (c) $\delta = 2$. The black solid curve shows the full solution (4.7), and the red dashed curve shows the approximate solution (3.1).

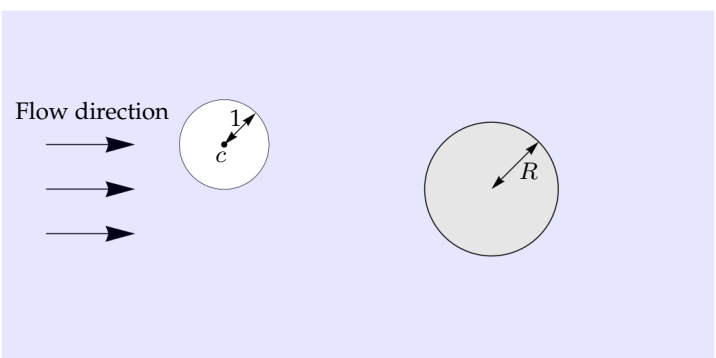

Figure 9. Schematic of the flow of a bubble past a circular obstacle (shown in grey).

(i) Solution

In this next example, we consider the flow of a bubble past a circular obstacle in a uniform outer flow of dimensionless magnitude 1. Again suppose the bubble centre is at $c \in \mathbb{C}$ with radius 1, and the obstacle is centred at the origin with radius R. The problem setup is shown schematically in figure 9.

It is straightforward to construct an approximate equation of motion for the bubble using the methodology laid out in §4. Without the bubble present, the complex potential $f(z)$ for flow around a circular obstacle is given by

$$f(z) = z + \frac{R^2}{z}. \tag{4.12}$$

The approximate bubble velocity $\mathcal{U}_{\text{approx}}$ is then given by (2.13), i.e.,

$$2\left(1 - \frac{R^2 c^2}{|c|^4}\right) = \mathcal{U}_{\text{approx}}\left(1 + \frac{1}{\delta|\mathcal{U}_{\text{approx}}|^{1/3}}\right). \tag{4.13}$$

The complex potential $w(z)$ for the full solution is a holomorphic function in the fluid domain, Ω, and satisfies the boundary conditions

$$\mathrm{Im}[w(z)] = q + \mathrm{Im}\left[\overline{\mathcal{U}}_b(z-c)\right] \qquad \text{on} \quad |z-c|=1, \tag{4.14a}$$

$$\mathrm{Im}[w(z)] = 0 \qquad \text{on} \quad |z|=R, \tag{4.14b}$$

$$w(z) \sim z \qquad \text{as} \quad z \to \infty. \tag{4.14c}$$

To solve (4.14) we adapt the methodology of [35] and conformally map from the solution domain, Ω, onto the concentric annulus $\mathcal{A} = \{\zeta : \mathcal{X} \le |\zeta| \le 1\}$ using the mapping

$$\zeta = \frac{1 - p(z-c)\mathrm{e}^{-\mathrm{i}\phi}}{(z-c)\mathrm{e}^{-\mathrm{i}\phi} - p}, \tag{4.15}$$

where $\phi = \pi + \arg(c)$ and

$$p = \frac{|c|^2 - R^2 + 1 - \sqrt{(|c|^2 - R^2 + 1)^2 - 4|c|^2}}{2|c|}, \tag{4.16a}$$

$$\mathcal{X} = p^2 + \frac{(R-1)p(p+1)(|c|-R-1)}{|c|(|c|-R-p)}. \tag{4.16b}$$

We then define $w(z) = z + W(\zeta)$, so that $W(\zeta)$ is holomorphic on $\mathcal{A}$, and satisfies the boundary conditions

$$\mathrm{Im}[W(\zeta)] = q + \mathrm{Im}\left[(\mathcal{U}_b - 1)\left(\frac{1+p\zeta}{\zeta+p}\right)\mathrm{e}^{\mathrm{i}\phi}\right] \qquad \text{on} \quad |\zeta|=1, \tag{4.17a}$$

$$\mathrm{Im}[W(\zeta)] = -\mathrm{Im}\left[\left(\frac{1+p\zeta}{\zeta+p}\right)\mathrm{e}^{\mathrm{i}\phi}\right] \qquad \text{on} \quad |\zeta|=\mathcal{X}. \tag{4.17b}$$

We expand $W(\zeta)$ as a Laurent series to obtain

$$W(\zeta) = \frac{(1-p^2)\mathrm{e}^{-\mathrm{i}\phi}}{p}\sum_{n=1}^{\infty}\frac{\mathcal{X}^n}{1-\mathcal{X}^{2n}}\left[\left((\overline{\mathcal{U}}_b - 1)\left(\frac{-p}{\mathcal{X}}\right)^n - \mathrm{e}^{2\mathrm{i}\phi}\left(\frac{-\mathcal{X}}{p}\right)^n\right)\zeta^n + \left((\mathcal{U}_b - 1)\mathrm{e}^{2\mathrm{i}\phi}(-p\mathcal{X})^n - \left(\frac{-\mathcal{X}}{p}\right)^n\right)\zeta^{-n}\right]. \tag{4.18}$$

Evaluating the left-hand side of the force balance (2.7) and using Cauchy's Residue Theorem we thus find

$$\frac{1}{\mathrm{i}\pi}\oint_{|z-c|=1} w(z)\,\mathrm{d}z = \frac{2(1-p^2)^2}{p^2}\sum_{n=1}^{\infty}\frac{n\mathcal{X}^{2n}}{1-\mathcal{X}^{2n}}\left[(1-\mathcal{U}_1)\left(\frac{p}{\mathcal{X}}\right)^{2n} - \mathrm{e}^{2\mathrm{i}\phi}\right]. \tag{4.19}$$

We can then write the equation of motion (2.7) as

$$f_2 - \frac{f_1 c^2}{|c|^2} = \mathcal{U}_b\left(f_2 - 1 + \frac{1}{\delta|\mathcal{U}_b|^{1/3}}\right), \tag{4.20}$$

where

$$f_1 = \frac{2(1-p^2)^2}{p^2}\frac{\Psi'_{\mathcal{X}^2}(1)}{4\log^2\mathcal{X}}, \tag{4.21a}$$

$$f_2 = \frac{2(1-p^2)^2}{p^2}\frac{\Psi'_{\mathcal{X}^2}\left(\frac{\log p}{\log \mathcal{X}}\right)}{4\log^2\mathcal{X}} \tag{4.21b}$$

are functions of $|c|$ and R.

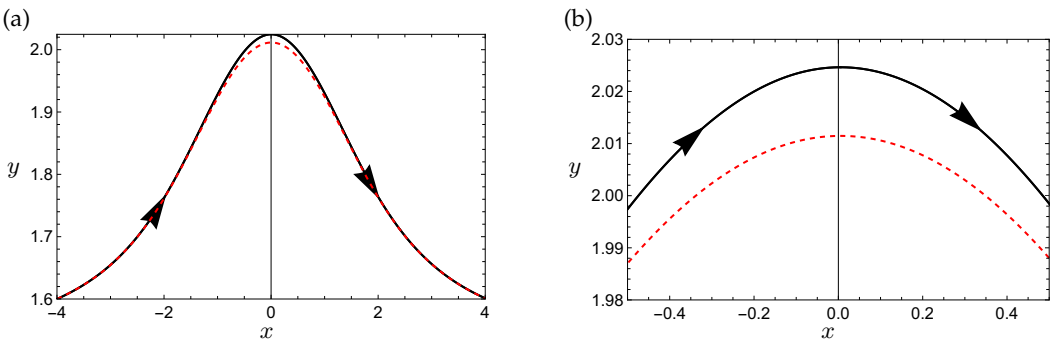

Figure 10. (a): A trajectory of (4.20) (black) with $\delta = 5$ and $R = 1$ and the corresponding streamline of the background flow (red, dashed). (b) The trajectory zoomed into the range $x \in [-0.5, 0.5]$.

(ii) Results

One can verify that $f_1 \sim 2R^2/|c|^2$ and $f_2 \to 2$ as $|c|/R \to \infty$, and the full equation of motion (4.20) thus reduces to the approximate version (4.13) when the bubble is far from the obstacle. However, similarly to §4(b), the solutions to (4.14) do not precisely follow the streamlines of the background flow, as is observed in figure 10. Here, the bubble deviates noticeably from its initial streamline only when the bubble is very close to the obstacle (see the close-up in figure 10(b)).

We can quantify the deviation from a streamline by defining a velocity ratio in the same manner as (4.9), that is,

$$U_{\text{ratio}} = \frac{V_b/U_b}{V_{\text{approx}}/U_{\text{approx}}} = \mathcal{F}\,\frac{\operatorname{Re}\left[1 - \frac{R^2c^2}{|c|^4}\right]}{\operatorname{Re}\left[1 - \frac{f_1 c^2}{f_2|c|^2}\right]}, \tag{4.22}$$

where the prefactor is given by

$$\mathcal{F} = \frac{f_1|c|^2}{f_2 R^2}. \tag{4.23}$$

From the above estimates for f_1 and f_2, we have that $\mathcal{F} \to 1$ and thus $U_{\text{ratio}} \to 1$ as $|c|/R \to \infty$, confirming that the bubble closely follows the streamlines of the background flow far from the obstacle. Indeed, we can use the quantity $\mathcal{F}$ as a measure of how closely the bubble follows the streamlines of the background flow, which is more useful than (4.22) because it is only a function of the distance $|c|$ (and the obstacle radius R).

We plot $\mathcal{F}$ versus $|c|$ in figure 11 for three different values of R. As $|c|$ decreases from $+\infty$, $\mathcal{F}$ increases from its limiting value of 1, approaching a finite limit as the bubble approaches the obstacle, namely

$$\mathcal{F} \to \frac{\pi^2(1+R)^2}{3R^2\,\mathcal{Z}\left(2, \frac{R}{1+R}\right)} > 1 \qquad \text{as} \quad |c| \to 1 + R, \tag{4.24}$$

where $\mathcal{Z}(s, b)$ is the Hurwitz zeta-function [36], defined by

$$\mathcal{Z}(s, b) = \sum_{n=0}^{\infty} \frac{1}{(n+b)^s}. \tag{4.25}$$

Thus we observe significant deviations from the background flow streamlines only when the bubble is close to the obstacle, as is seen in figure 10(b). Furthermore, those deviations are more noticeable for smaller values of the obstacle radius R.

As in §3(a), we observe a mild (square root) singularity in the function $\mathcal{F}$ as the distance $|c| - R - 1$ of the bubble from the obstacle tends to zero, but this repulsive effect is too weak to prevent a finite-time collision. However, for suitably chosen initial conditions, it is possible for the bubble

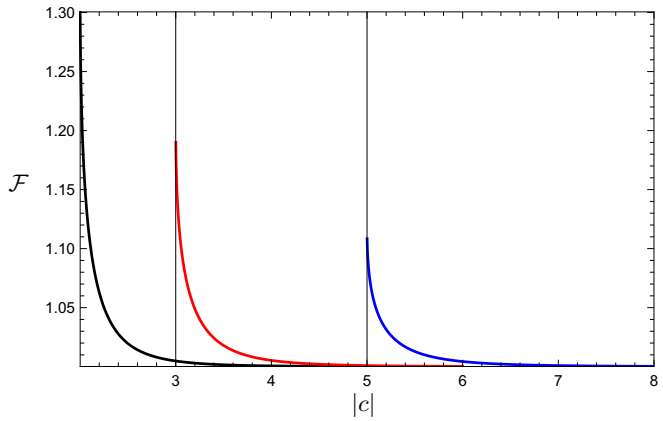

Figure 11. Velocity ratio function $\mathcal{F}$ versus centre–centre distance from the bubble to the obstacle, $|c|$, for $R=1$ (black), 2 (red), 4 (blue).

to safely navigate past the obstacle. In figure 12(a), we plot the time, T, taken for the bubble to traverse around the obstacle versus δ for two such cases, starting at $z=-x_0+\mathrm{i}y_0$ and ending at $z=x_0+\mathrm{i}y_0$. Specifically, we choose $(x_0,y_0)=(4,1.6)$ when $R=1$, and $(x_0,y_0)=(5,1.95)$ when $R=2$. We find that T is a monotonically decreasing function of δ, as expected, since the bubble speed increases with δ. We also observe that the approximate solution (4.13) closely matches the full solution (4.20), slightly over-predicting T for $\delta<1$ and under-predicting for $\delta>1$. (Similar qualitative changes in behaviour as δ passes through 1 were found by [7]).

In figure 12(b) we plot the normalised difference, $(T-T_{\mathrm{approx}})/T_C$, between the full solution and the approximate solution, versus δ. The characteristic time-scale is taken to be the time for a bubble to travel the diameter of the obstacle if the obstacle was not present, i.e., $T_C=2R/\tilde{U}_b$, where $\tilde{U}_b$ is given by the solution of (2.16). This normalisation takes into account variations in the transit time arising solely from the dependence of the isolated bubble speed on δ, and we observe in figure 12(b) that it approximately collapses the data for different values of the obstacle radius R. We also observe that the switch from the approximate solution under-estimating to over-estimating the transit time occurs close to but not precisely at $\delta=1$. Overall, despite the significant deviations between the approximate and full solutions for the velocity when the bubble is very close to the obstacle, the total transit time T is affected only slightly, because the bubble is very close to the obstacle only briefly. In both examples considered here, we find that the bubble is within 0.1 radius of the obstacle less than 15% of the time, regardless of the value of δ.

In the same manner as (4.10) we define the maximum relative error as

$$\mathrm{Error}(|c|,R)=\max_{\arg c\in[0,2\pi)}\frac{|\mathcal{U}_b-\mathcal{U}_{\mathrm{approx}}|}{|\mathcal{U}_b|}. \tag{4.26}$$

We plot (4.26) versus δ, for $R=1$ and various values of $|c|$ in figure 13(a) and for $|c|=1+R$ and various values of R in figure 13(b). We find that the maximum error occurs at $|c|=1+R$, as expected, and it quickly decreases with increasing $|c|$. Also, the error increases with the obstacle radius, R. For small values of δ, the error is a decreasing function of δ, while for large values it is an increasing function, with a non-smooth transition between the two behaviours. Similarly to §4(b)ii, this switch in behaviour occurs when the location of the maximum error jumps from $\arg c=\pm\pi/2$ to $\arg c=0$.

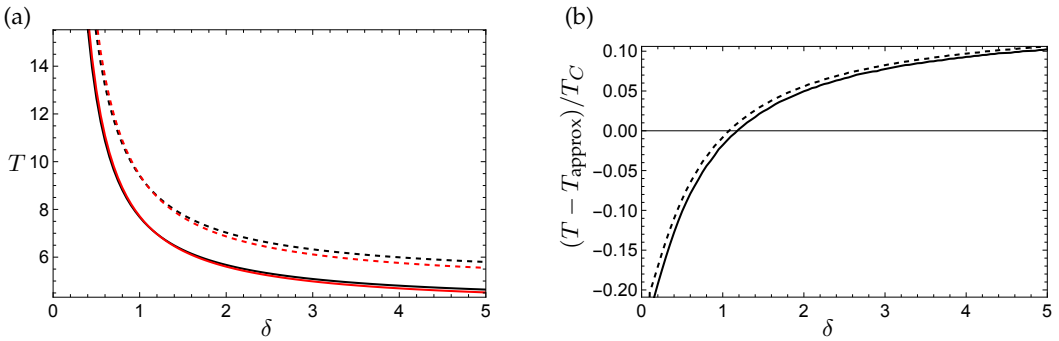

Figure 12. (a) Time taken, T for the bubble to travel around the obstacle at $|z| \leq R$ for the full solution (black) and the approximate solution (red) versus δ, with (solid) $R = 1$ and the bubble centre initially at $z = -4 + 1.6\mathrm{i}$, and ending at $z = 4 + 1.6\mathrm{i}$, (dashed) $R = 2$ and the bubble centre initially at $z = -5 + 1.95\mathrm{i}$, and ending at $z = 5 + 1.95\mathrm{i}$. (b) The normalised difference, $(T - T_{\text{approx}})/T_C$, between the full solution and the approximate solution, versus δ, for $R = 1$ (solid) and $R = 2$ (dashed). The normalisation constant $T_C = 2R/\tilde{U}_b$, where $\tilde{U}_b$ is given by the solution of (2.16).

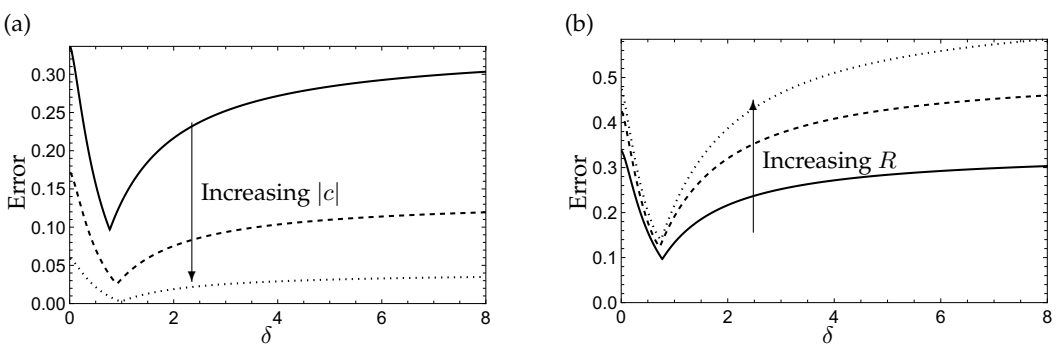

Figure 13. The maximum error in the bubble velocity versus δ for flow past a circular obstacle: (a) with $R = 1$ and $|c| = 2$ (solid), 2.1 (dashed), 2.5 (dotted); (b) with $|c| = 1 + R$ and $R = 1$ (solid), 2 (dashed), 4 (dotted).

5. Conclusions

In this paper, we model the motion of a bubble in a non-uniform flow in a Hele-Shaw cell. We consider the distinguished limit where the bubble aspect ratio, ϵ, and the capillary number, Ca, are both small, with the so-called Bretherton parameter $\delta = \mathrm{Ca}^{1/3}/\eta\epsilon = O(1)$ (where $\eta \approx 0.893$ is a constant) In this regime, the bubble is approximately circular and its velocity is determined by a net force balance. We thus find a general equation of motion for such a bubble in an arbitrary external flow. We apply the theory to study the motion of a bubble in a stagnation-point flow, and between a source and a sink, situations that occur abundantly in microfluidic devices.

For the simplest nontrivial case of a uniform external flow, the theory reproduces the result obtained previously by Booth *et al.* [7]: the bubble travels parallel to the background flow, and its relative speed is determined as a function of δ. We find that the same holds true for a general background flow: the bubble travels parallel to the *local* velocity, and its relative speed is determined by the same function of the *local* Bretherton parameter, which is defined using the external flow speed evaluated at the bubble centre. Hence, the bubble centre travels along a streamline of the background flow that would exist if the bubble was not present. The bubble thus acts somewhat like a tracer particle, albeit one that travels at a speed different from the background flow speed.

Next, we use the same methodology to derive an approximate equation of motion for a bubble in a more complicated domain including walls or obstacles. The strategy is to find the complex potential of the background flow without the bubble present and then simply substitute this

potential into our general equation of motion. This approximation ignores second-order image effects from interaction between the bubble and any boundaries present, similarly to the dipole approximations used to study the motion of bubbles in a uniform background flow [26,31,33]. In this approach, the complex potential of the background flow, and hence the equation of motion for the bubble, can be derived once and for all, whereas, in the full solution, one would need to recalculate the complex potential at each time step.

We compare the approximate solution with the full analytical solution in two test cases: a stagnation point on a wall, and flow around a circular obstacle. In both cases, the approximate solution for the bubble velocity proves to be remarkably accurate unless the bubble is extremely close to the obstacle. We devise the diagnostic functions U_{ratio} and $\mathcal{F}$ that allow the accuracy of the approximate solutions to be quickly assessed. As shown in figure 5, the approximate and full solutions for the stagnation point flow are within 5% of each other provided the bubble is more than 0.3 radii away from the wall. Similarly, figure 11 shows that the approximate solution for flow past a circular obstacle differs from the full solution by less than 5% provided the bubble is more than 0.2 radii from the obstacle. Furthermore, the bubble tends to be that close to the obstacle only briefly (if at all). We can thus obtain generally good approximations for the bubble trajectories and, e.g., the time taken for the bubble either to hit or to pass by the obstacle (see figures 6 and 12).

Our model neglects the leakage of fluid into and out of the thin films between the bubble and the cell walls. This effect causes small corrections to the kinematic boundary condition (2.4), which can be incorporated into our model as shown in [30]. We note also that, as the bubble approaches a wall or an obstacle, the Hele-Shaw model will ultimately break down when the distance from the boundary becomes comparable to the cell height. To describe the final stages of collision or a near-miss, a three-dimensional analysis would need to be conducted in the thin gap between the bubble and the boundary.

The results presented in this paper provide a framework to study the dynamics of bubbles in a wide variety of background flows found in microfluidic devices. In principle, the technique could be extended to include multiple bubbles, by following the conformal mapping techniques used in [35] for the motion of two bubbles or the Schottky-Klein prime function approach developed by Crowdy [17,37,38] for a general number of bubbles.

Acknowledgements. DJB is grateful to EPSRC, grant reference number EP/V520202/1, for funding.

References

1. Anna SL. 2016 Droplets and bubbles in microfluidic devices. *Ann. Rev. Fluid Mech.* **48**, 285–309.
2. Huerre A, Miralles V, Jullien MC. 2014 Bubbles and foams in microfluidics. *Soft Matter* **10**, 6888–6902.
3. Garstecki P, Gitlin I, DiLuzio W, Whitesides GM, Kumacheva E, Stone HA. 2004 Formation of monodisperse bubbles in a microfluidic flow-focusing device. *Appl. Phys. Lett.* **85**, 2649–2651.
4. Prakash M, Gershenfeld N. 2007 Microfluidic bubble logic. *Science* **315**, 832–835.
5. Zhu L, Gallaire F. 2016 A pancake droplet translating in a Hele-Shaw cell: lubrication film and flow field. *J. Fluid Mech.* **798**, 955–969.
6. Reichert B, Huerre A, Theodoly O, Valignat MP, Cantat I, Jullien MC. 2018 Topography of the lubrication film under a pancake droplet travelling in a Hele-Shaw cell. *J. Fluid Mech.* **850**, 708–732.
7. Booth DJ, Griffiths IM, Howell PD. 2023 Circular bubbles in a Hele-Shaw channel: a Hele-Shaw Newton's cradle. *J. Fluid Mech.* **954**, A21.
8. Taylor G, Saffman PG. 1959 A note on the motion of bubbles in a Hele-Shaw cell and porous medium. *Q. J. Mech. Appl. Math.* **12**, 265–279.
9. Saffman P. 1959 Exact solutions for the growth of fingers from a flat interface between two fluids in a porous medium or Hele-Shaw cell. *Q. J. Mech. Appl. Math.* **12**, 146–150.
10. Tanveer S. 1986 The effect of surface tension on the shape of a Hele-Shaw cell bubble. *Phys. Fluids* **29**, 3537–3548.
11. Maxworthy T. 1986 Bubble formation, motion and interaction in a Hele-Shaw cell. *J. Fluid Mech.* **173**, 95–114.

12. Acheson D. 1990 *Elementary Fluid Dynamics*. Oxford University Press.
13. Howison S. 1986 Fingering in Hele-Shaw cells. *J. Fluid Mech.* **167**, 439–453.
14. Howison S. 1992 Complex variable methods in Hele-Shaw moving boundary problems. *European Journal of Applied Mathematics* **3**, 209–224.
15. Cummings L, Howison S, King J. 1999 Two-dimensional Stokes and Hele-Shaw flows with free surfaces. *Eur. J. Appl. Math.* **10**, 635–680.
16. Gustafsson B, Vasil'ev A. 2006 *Conformal and potential analysis in Hele-Shaw cells*. Springer Science & Business Media.
17. Crowdy DG. 2009 Multiple steady bubbles in a Hele-Shaw cell. *Proc. R. Soc. Lond. A* **465**, 421–435.
18. Andersen C, Lustri CJ, McCue SW, Trinh PH. 2024 On the selection of Saffman–Taylor viscous fingers for divergent flow in a wedge. *J. Fluid Mech.* **987**, A42.
19. Bretherton F. 1961 The motion of long bubbles in tubes. *J. Fluid Mech.* **10**, 166–188.
20. Meiburg E. 1989 Bubbles in a Hele-Shaw cell: Numerical simulation of three-dimensional effects. *Phys. Fluids A* **1**, 938–946.
21. Tan J, Xu J, Li S, Luo G. 2008 Drop dispenser in a cross-junction microfluidic device: Scaling and mechanism of break-up. *Chem. Eng. J.* **136**, 306–311.
22. Leshansky A, Pismen L. 2009 Breakup of drops in a microfluidic T junction. *Phys. Fluids* **21**.
23. Garstecki P, Fuerstman MJ, Stone HA, Whitesides GM. 2006 Formation of droplets and bubbles in a microfluidic T-junction—scaling and mechanism of break-up. *Lab Chip* **6**, 437–446.
24. Gaillard A, Keeler JS, Le Lay G, Lemoult G, Thompson AB, Hazel AL, Juel A. 2021 The life and fate of a bubble in a geometrically perturbed Hele-Shaw channel. *J. Fluid Mech.* **914**, A34.
25. Gnyawali V, Moon B, Kieda J, Karshafian R, Kolios M, Tsai S. 2017 Honey, I shrunk the bubbles: microfluidic vacuum shrinkage of lipid-stabilized microbubbles. *Soft Matter* **13**, 4011–4016.
26. Shen B, Leman M, Reyssat M, Tabeling P. 2014 Dynamics of a small number of droplets in microfluidic Hele-Shaw cells. *Exp. Fluids* **55**, 1–10.
27. Wu K, Booth DJ, Griffiths IM, Howell PD, Nunes JK, Stone HA. 2024 The motion and deformation of a bubble in a Hele-Shaw cell. *Phys. Rev. Fluids* **9**, 123603.
28. Park CW, Homsy G. 1984 Two-phase displacement in Hele-Shaw cells: theory. *J. Fluid Mech.* **139**, 291–308.
29. Peng G, Pihler-Puzović D, Juel A, Heil M, Lister J. 2015 Displacement flows under elastic membranes. Part 2. Analysis of interfacial effects. *J. Fluid Mech.* **784**, 512–547.
30. Burgess D, Foster MR. 1990 Analysis of the boundary conditions for a Hele-Shaw bubble. *Phys. Fluids A* **2**, 1105–1117.
31. Beatus T, Tlusty T, Bar-Ziv RH. 2006 Phonons in a one-dimensional microfluidic crystal. *Nat. Phys.* **2**, 743–748.
32. Keeler JS, Thompson AB, Lemoult G, Juel A, Hazel AL. 2019 The influence of invariant solutions on the transient behaviour of an air bubble in a Hele-Shaw channel. *Proc. R. Soc. Lond. A* **475**, 20190434.
33. Beatus T, Bar-Ziv RH, Tlusty T. 2012 The physics of 2D microfluidic droplet ensembles. *Phys. Rep.* **516**, 103–145.
34. Salem A. 2012 A completely monotonic function involving q-gamma and q-digamma functions. *J. Approx. Theory* **164**, 971–980.
35. Booth DJ, Wu K, Griffiths IM, Howell PD, Nunes JK, Stone HA. 2024 Bubble racing in a Hele-Shaw cell. *Submitted to J. Fluid Mech.*.
36. Kanemitsu S, Katsurada M, Yoshimoto M. 2000 On the Hurwitz–Lerch zeta-function. *Aequ. Math.* **59**, 1–19.
37. Crowdy DG. 2020 *Solving problems in multiply connected domains*. SIAM.
38. Crowdy DG. 2016 Uniform flow past a periodic array of cylinders. *Eur. J. Mech. B. Fluids* **56**, 120–129.